Instrumentation for fast functional optical tomography

Christoph H. Schmitz, Mario Löcker,[a] Joseph M. Lasker,[b] Andreas H. Hielscher,[b],[c] and Randall L. Barbour[c],[d]

Department of Pathology, SUNY Downstate Medical Center, Box 25, 450 Clarkson Avenue, Brooklyn, New York 11203

In this article, we describe the design rationale and performance features of an integrated multichannel continuous wave (cw) near-infrared (NIR) optical tomographic imager capable of collecting fast tomographic measurements over a large dynamic range. Fast data collection ($\sim$70 Hz/channel/wavelength) is achieved using time multiplexed source illumination (up to 25 illumination sites) combined with frequency encoded wavelength discrimination (up to four-wavelength capability) and parallel detection (32 detectors). The described system features a computerized user interface that allows for automated system operation and is compatible with various previously described measuring heads. The results presented show that the system exhibits a linear response over the full dynamic measuring range (180 dB), and has excellent noise ($\sim$10 pW noise equivalent power) and stability performance ($<$1% over 30 min). Recovered images of laboratory vessels show that dynamic behavior can be accurately defined and spatially localized. © *2002 American Institute of Physics.* [DOI: 10.1063/1.1427768]

I. INTRODUCTION

In recent years, diffuse optical tomography has become a viable new biomedical imaging modality. The appeal of this method lies in the use of nonionizing radiation, the ability to probe functional states of tissue, and the use of economical and compact instrumentation. The technique typically employs laser diodes that deliver light through optical fibers to several locations on the tissue surface, and measurements of back-reflected and transmitted light intensities are recorded and analyzed. Tomographic reconstruction algorithms provide the spatial distribution of optical properties or changes of these properties for the site under investigation. A number of studies have shown that the resulting parameter maps can be used to detect breast cancer,[1,2] brain activity,[3–5] and other clinically relevant findings.[6–8]

Several groups have developed instrumentation for optical tomography over the last eight years. Depending on the temporal characteristics of the illumination source, instrumentation can be categorized into systems that use ultrashort laser pulses (time-domain measurements), rf-modulated light sources (frequency-domain measurements), or low-frequency (dc to $\sim$kHz) modulated light sources (continuous wave (cw) measurements). Examples of time-resolved instrumentation have been described by Ntziachristos *et al.*[9] and Schmidt *et al.*[10] Frequency-domain instrumentation has been developed by Pogue,[2] Jiang,[11] and groups led

by Sevick-Muraca[12] and Gratton.[13] Among others, Siegel *et al.*,[14] Zhao *et al.*,[15] Yamashita *et al.*,[16] and our group[17,18] have focused on the development of high fidelity cw instrumentation.

The advantages and disadvantages of these various approaches have been discussed in detail elsewhere.[19] While time-resolved and frequency-domain methods can provide data having richer information content, we nevertheless favor cw measurements in recognition of advantages that are related to cost/performance issues. These include the ease by which fast parallel measurements can be accomplished while retaining a large dynamic range. Recently, we have emphasized that such capabilities, adapted to imaging studies, allow for the investigation of an entirely new class of information about tissue function—that associated with the natural spatial and temporal heterogeneity of the vascular response in large tissue structures.[20]

In this article, we build on our previous work towards developing instrumentation well suited for dynamic imaging. In particular, we expand on a design concept that employs silicon photodiodes as optical detectors,[18] which overcomes the limitations of a charge coupled device based imager described earlier.[17] Advantages include eliminating sensitivity to ambient light, fast source switching, and simultaneous multiwavelength measurements. Here, we describe the performance features of a fully integrated measuring system. A preliminary report of this has recently been given.[21]

II. INSTRUMENT DESIGN

The system developed is based on a design that provides for fast parallel data capture with a large dynamic range and employs dc illumination.[18] Guiding our approach has been the goal of engineering a unit that provides for automated
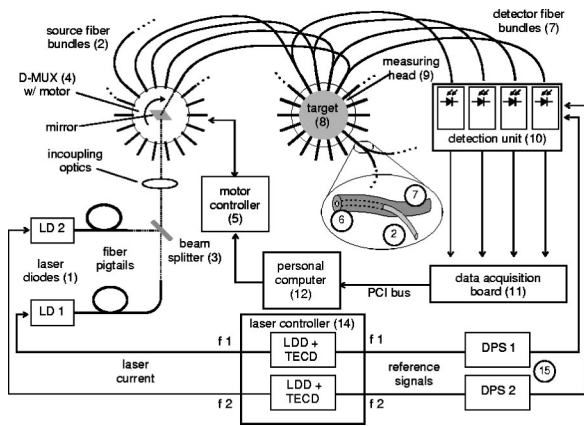

FIG. 1. Block diagram of the instrument setup. LDD: laser diode drivers, TECD: thermo-electric cooling drivers, $f1$ and $f2$: diode current modulation frequencies, LD1 and LD2: laser diodes, D-MUX: optical demultiplexer with servomotor, DPS1 and DPS2: digital phaseshifters.
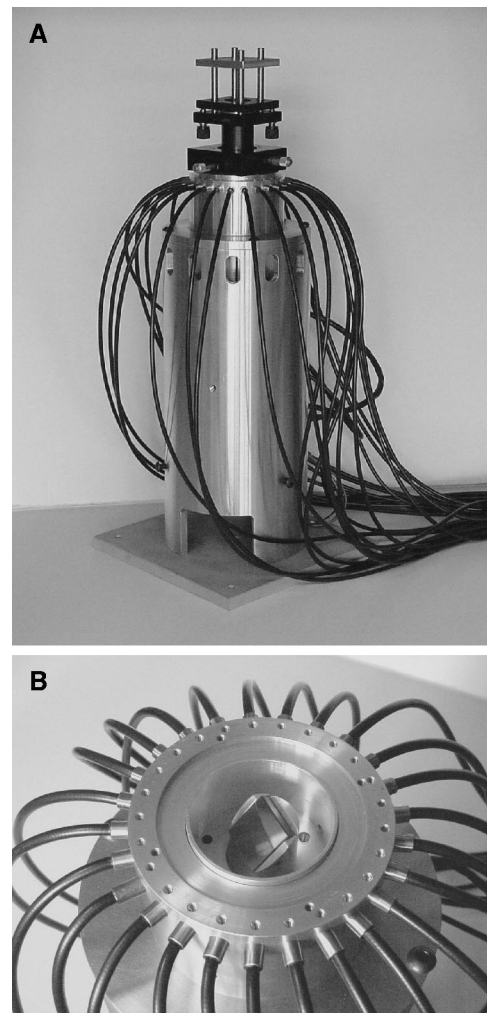

FIG. 2. Photograph of the optical D-MUX. (a) Complete view of the unit (height ~15 in.) with optical fibers attached to it. (b) Detailed view of the rotating mirror with the in-coupling optics removed.

instrument setup and control as well as to introduce performance features that facilitate the development and evaluation of experimental protocols focused on the measurement of evoked vascular responses.[21] This includes the integration of system software that allows for online viewing of collected data within various formats as well as the online reconstruction and display of image parameter maps. Here, we restrict our focus to presenting the results that define the system hardware performance. Descriptions of our algorithms for image formation and other features related to system functionality are described elsewhere.[22]

Figure 1 shows a block diagram of the instrument whose design rationale was previously described[18] but not reduced to practice within an integrated system. The system couples light from two (or more) laser diodes (1) operating in the 800 nm range into one of multiple source fiber bundles (2). Several options are available to render the incident beams collinear. For convenience, we simply use a nonpolarized beam splitter (3). Fast switching between source fiber bundles is made possible by means of an optical demultiplexer (D-MUX, 4).

This unit, to be described more fully, employs a brushless dc servomotor to provide for fast, precise source beam positioning. The motor is driven by a controller (5) containing a freely programmable microprocessor. Each source fiber bundle (1-mm-diam., 2) forms one branch of a bifurcated fiber bundle (6) and joins the other branch (3-mm-diam., 7), which is used for light collection on the target surface (8). These are housed within one of several measuring heads (9) that have the property of establishing stable optical contacts with tissues of various size and shapes.[18] Each of the detector fiber bundles terminates at one silicon photodiode measuring sensor of a multichannel detection unit (10). The output voltages of the detector channels are measured by means of a data acquisition (DAQ) board (11) and stored on a personal computer (PC, 4). For the purpose of lock-in detection, the laser diodes are current modulated in the 5–10 kHz range by the laser controller (14), and digital phase shifters (15) are used to optimize the phase angle between the measured and reference signals.

A. Light source

We use high-power laser diodes (LD), with integrated thermo-electric cooling (TEC), that are optically coupled to the D-MUX by means of a pigtailed fiber to which is attached a gradient index lens that serves to produce a substantially collimated beam. The laser diodes (high power devices 1110-BUTF-TEC) operate in the 800 nm region and have a maximum optical output power of 400 mW at the distal end of the fiber. These are typically operated at a mean optical output power of 100 mW; the optical power incident on the target is about 30 mW. The lasers are operated by a Newport model 8000 laser controller mainframe housing up to four combined LD/TEC driver modules (model 8630), each serving one laser. Each module provides sinusoidal modulation of the LD current with individually selectable frequency and amplitude. The modules also generate reference signals at transistor–transistor logic (TTL) level, which are supplied by coaxial BNC connectors on the real panel of the unit.

Figure 2 shows a detailed view of the D-MUX. The unit houses a brushless dc servomotor that moves a gold-surfaced mirror, mounted 45° to its shaft, in a start–stop fashion. It is essential that the mirror make a complete stop for a short

time (~10 ms) in order to minimize degradation of the precision of the system due to variations in light intensity during the detection process. The selected motor (Pacific Scientific model R23GENA-RS-NS-01) and accompanying microprocessor control unit (Pacific Scientific model SC902AN-001-01) allow for the flexible implementation of the customized motion control protocols. This unit is capable of performing ~75, 14° start–stop motions per second without noticeable overshooting or ringing. The D-MUX unit currently in use houses up to 25 source fiber bundles that are available for target illumination. The software-programmable motor controller allows absolute indexing of the motor position and easy implementation of complex motion protocols. This allows for user selection of the number, timing, and order of source fibers used for target illumination. Because the maximum switching speed between two source positions has an upper limit, increasing the number of sources will reduce the image-framing rate. For example, with 17 source positions and a 50 Hz switching rate, ~3 full tomographic data sets per second can be acquired. As described in a recent article,[18] we have chosen to implement a time-multiplexing scheme instead of a previously described frequency-multiplexing scheme[14] in order to maximize the dynamic measuring range. This serves to enhance the view over which larger structures can be examined.

B. Measuring heads

One of the instrumentation challenges of optical tomography as a medical imaging modality is interfacing the apparatus with the tissue under investigation. Because the intensity of light exiting the tissue falls exponentially with distance from the source, a tomographic measurement often requires the detection of faint signals. In order to maximize the signal-to-noise ratio, mostly contact-based measurements, usually using optical fibers, are employed. This immediately presents a challenge of how to accomplish this given the contradictory demands between the variable size and geometry of human anatomy and the need for a flexible yet mechanically stable interface. Our approach has been to provide different interchangeable measuring heads for different basic geometries. The rationale and design of several available devices—including an iris-like structure, well-suited for imaging structures of circular cross section such as a limb, a flexible pad for planar sites, and a folding hemisphere for breast imaging—have been described in detail earlier.[18] We have recently added a wristband-like interface for limb imaging and a helmet device suited for transcranial investigations. Common to all of these devices is their ability to adapt to various target sizes while providing stable optical contact.

Our experience with these has been that by adjusting their fit to provide for modest contact pressure together with having the fiber ends protrude from the measuring head by ~1–2 mm, stable and reliable contact throughout the measurement is maintained. This is evidenced by the absence of any sudden changes in detector responses as one might expect would occur should unstable contact be present, and by the depressions in the skin that are seen upon removal of the
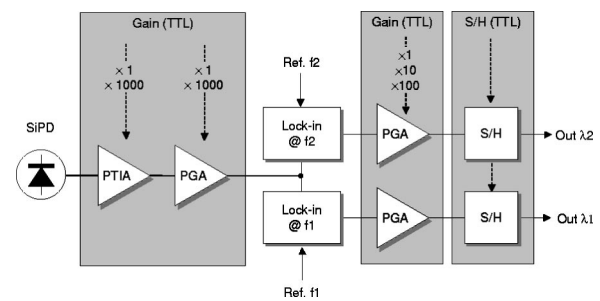

FIG. 3. Block diagram of detector channel. SiPD: silicon photodiode, PTIA: programmable transimpedance amplifier, PGA: programmable gain amplifier, Ref. f1, Ref. f2: Reference signals, S/H: sample-and-hold, Out λ1 and Out λ2: Output signals for different wavelengths; Gain (TTL), S/H (TTL): Digital control signals.

device. We recognize consideration of the homogeneity of optical coupling to tissue can having significant implications for how the acquired data should be evaluated. It is for this reason that we employ reconstruction methods that evaluate a relative change in detector responses, rather than assuming absolute calibrations can be reliably obtained. In this fashion, each channel is referenced to itself, thereby rendering our imaging schemes insensitive to possible differences in coupling efficiencies among the fibers.

C. Detection

Figure 3 shows a block diagram of one detector channel. We have selected a silicon photodiode (SiPD) as the photosensor because of its excellent linearity (better than $1:10^{10}$), high sensitivity (noise equivalent power $=6.5 \times 10^{-15}$ W Hz$^{-1/2}$), and ease of operation. The rationale and design of the detection electronics have been recently described in detail in a report by Schmitz *et al.*[18] Motivating our approach was the need to achieve fast detection over a large dynamic range, coupled with fast source switching. This is achieved by synchronizing adjustment of the detector sensitivity for all channels with source movement, thereby achieving on-the-fly adaptive gain control.

Briefly, the signal amplification scheme used converts the photocurrent generated by the incident light to a voltage by means of a programmable transimpedance amplifier (PGIA) whose transimpedance value (gain), and hence photosensitivity, can be changed by a factor of 1000. Subsequently, a programmable gain amplifier (PGA) can be set to either a gain of unity or an additional factor of one thousand. Following appropriate amplification, the signal is fed to one or more lock-in amplifiers [(LIAs), two are shown] to remove dc offsets, signals from ambient light, and electronic noise. By modulating the lasers at distinct frequencies, different wavelengths of light, simultaneously measured, can be distinguished.

Sample-and-hold circuits (S/H) are used to permit parallel data capture and to facilitate system timing. A second PGA located prior to each S/H circuit allows for adjusting the level of the demodulated (dc) signal, thereby improving noise immunity when transmitting analog signals to the data acquisition board. This also serves to effectively increase the usable dynamic range of the analog-to-digital conversion.
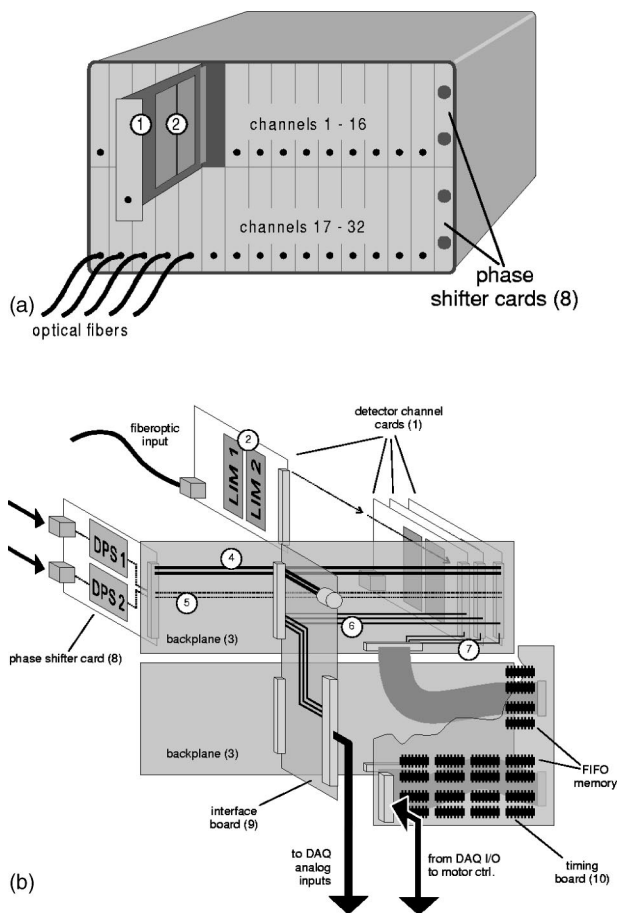
FIG. 4. Panel A. Schematic of the detection unit with detector channels. Panel B. Rear exploded view of detection unit without external chassis. (2) LIM 1, LIM 2: lock-in amplifier modules, (4) supply voltage line, (5) reference signal, (6) read-out lines, (7) gain control lines, DPS1 and DPS2: digital phase shifters, DAQ: data acquisition board, and FIFO: first-in-first-out.

The amplified signal is then transmitted to a 64-channel data acquisition board (National Instruments model PCI-6033E) allowing the simultaneous readout of 32 detector channels at two wavelengths. This board also provides eight programmable digital input/output (I/O) ports, which are used for system control and timing (see Sec. I D 2). The board is fully compatible with National Instruments' LABVIEW™ software, which was used to create an interactive graphical control interface for the instrument.

It is worth noting that the design approach of gain switching, coupled with use of multiple simultaneous illuminating sources, assumes that the measured signal intensities for any one source-detector pair are largely independent, within an order of magnitude, of the illuminating wavelengths used. We also note that whereas this holds for tissue studies in the near-infrared (NIR) wavelength region, it may not be suitable in cases where the target optical properties exhibit strong wavelength dependence. In such cases, a selected gain setting suitable for one illuminating wavelength may either saturate or insufficiently amplify a measured signal.

Figure 4 shows a schematic of the multichannel detection unit. Panel A illustrates a front view, and panel B shows an exploded rear view absent the external chassis. The device
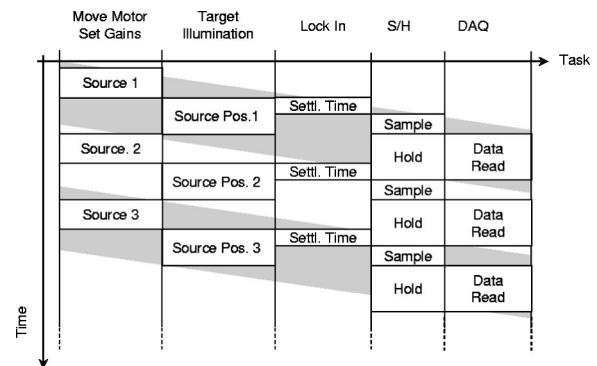

FIG. 5. System timing diagram.

is capable of measuring up to 32 channels in parallel. Each detector channel card (1) can be equipped with either one or two lock-in amplifier modules (2), each carrying two LIAs. This allows for the simultaneous measurement of as many as four different light sources. Each detector channel is connected to a backplane (3), which provides supply voltages (4), reference signals (5), read-out lines (6), and gain control signals (7). Depending on the number of modulation frequencies used, up to two phase shifter cards (8) can be inserted, each containing two digital phase shifters. The detection unit also contains an interface board (9) that serves to connect analog and digital ports from other hardware used in the instrument (DAQ board, power supply, and motor controller). The detection unit also contains a system timing board (10) that serves to store predetermined gain settings and establishes two-way communication with the motor controller unit.

D. System timing

1. Timing scheme

Precise instrument timing is crucial for the applications we seek to pursue, because many different system tasks have to be scheduled in a way that allows for maximum image framing rates without sacrificing measurement precision. Figure 5 shows schematically how the different system tasks proceed in time as the sources are switched. Tasks that have to be scheduled are: servomotor positioning, parallel multichannel light detection, and data capture.

Optical signal detection is performed for all detectors in parallel, to maximize the achievable frame rate. The detection process for an individual detector channel is composed of three subtasks: setting the detector to the appropriate gain, allowing the lock-in amplifier to settle, and triggering the S/H circuit. Adjusting the gain setting for each detector with respect to each source position is crucial because this provides the dynamic measurement range that is necessary to allow for high-quality signals when probing large tissue structures. Switching of these is achieved in a time well below 1 ms.

A measurement cycle begins by initiating the motor movement to the next stop (source) position and setting the detectors to the appropriate gain for that source position. After the mirror has stopped at its new position, the actual measuring process, i.e., the settling of the LIAs, takes place.
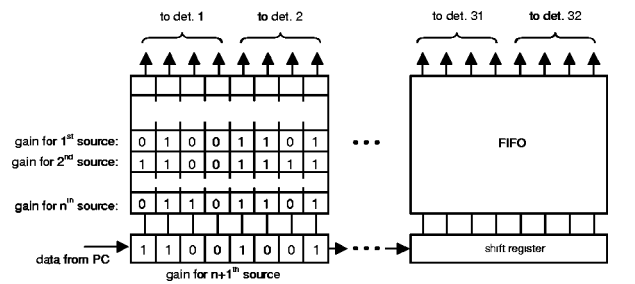
FIG. 6. Use of shift registers and FIFO memory for transmitting and storing gain settings for each source-detector pair.

The choice of a settling time (or detection bandwidth) for a LIA is always a tradeoff between instrument response (ideally immediate, i.e., fast-settling LIA) and the signal-to-noise ratio [(SNR), which should be large, i.e., slowly settling LIA]. The consequences of this tradeoff for our application have been discussed in detail,[18] and have led to a LIA design with a settling time of $6-7$ ms. After this amount of time has elapsed, the S/H circuit is triggered, thereby freezing the signal level. This is followed by allowing the motor to proceed to the next position, while the detector channels are simultaneously read out by the data acquisition board. Depending on the number of detector channels/wavelengths used, this can require up to ~ 1 ms to complete. The entire cycle is repeated according to a preselected number of acquisition time points, at a rate on the order of 75 Hz.

2. Hardware implementation

The main timing challenge in our system is the fast simultaneous switching of gain settings for all detector channels synchronously with the motor movement and data acquisition. We adopted two principal strategies to achieve this: First, we have chosen to use the motor controller as the clock for the timing of the system tasks. In this manner, we avoid burdening the host PC, which—as a Microsoft Windows-based system—is not well suited for real-time applications. The motor controller contains several freely programmable digital I/O lines that allow synchronized communication of the motion protocol with the external hardware. Secondly, we predetermine the gain settings for all source-detector pairs prior to a measurement (see Sec. II D) and store them temporarily in volatile memory located within the detection unit. Every detector channel requires four bits to determine its gain setting, leading to a total of 128 bits for a 32-channel module. Transmitting this information directly from the host PC to the detection module "on the fly," i.e., synchronously with the switching of source positions, would pose a nontrivial hardware-timing problem.

Instead, we use a combination of digital shift registers and first-in-first-out (FIFO) memory to transmit the gain settings, as determined from an initial measurement, to the detection hardware and store them temporarily (see Fig. 6). The shift registers allow the streaming of information at a moderate speed over a single serial line. This avoids the need for a complex handshaking scheme should the suggested rapid on-the-fly protocol be attempted. The parallel outputs of the shift registers are connected to the data inputs of 8-bit-wide
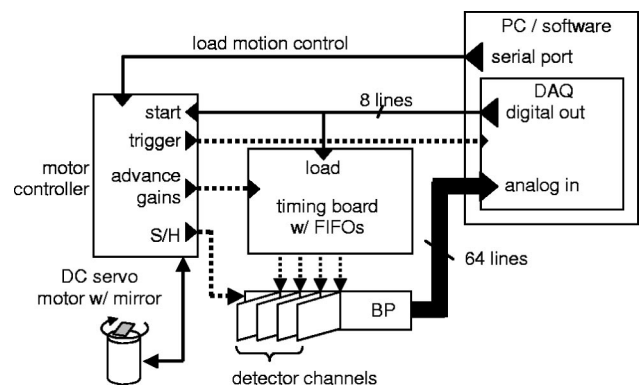

FIG. 7. Hardware communication layout. BP: backplane and DAQ: data acquisition board.

FIFO buffers, which store groups of eight bits, each encoding the gain setting of two detector channels for one source position. Thus, the bit combinations encoding the gains for successive source positions are "stacked" in the order that they are demanded during the measurement. The unique feature of a FIFO buffer (as opposed to a random access memory or a last-in-first-out memory) is the ability to retrieve the stored information in the order it has been stored by applying a digital impulse to the device. The FIFO data outputs are connected to the detector channels. After all source positions have been cycled through, a digital impulse notifies the memory chip to restart, repeating the sequence. In this fashion, the FIFO memory acts as a circular buffer, thereby avoiding the need to store gain settings for each time point of the measurement sequence. Because the FIFO memory does not require explicit data addressing, the timing for this scheme is very simple and efficient.

The hardware communication layout is shown as a block diagram in Fig. 7. The program for the motion control protocol is downloaded from the PC to the motor controller, which then waits idly until one of its control inputs is addressed by one of the digital I/O lines provided by the multifunction DAQ board. These I/O lines are also used to transmit the gain settings for each source-detector combination to the timing board, where they are stored in FIFO buffers prior to measurement.

The measurement is started by initiating a digital input signal from the DAQ board to the motor controller, which then executes the motion program for as long as the input remains in the activated state. The motor controller starts the mirror movement and then sends out a digital pulse that triggers the FIFO buffers, thereby advancing the gain settings. After the mirror has reached the desired source position, the motion control program allows the appropriate time for the LIAs to settle (~ 7 ms) and then triggers the S/H circuit and the data acquisition.

E. Instrument control

All instrument control is accomplished through a graphical user interface created with LABVIEW™ software. An important and potentially tedious task, should it be implemented using manual methods, is the determination of the appropriate gain settings for all source-detector combina-

tions. Which gain settings are appropriate depends on the particulars of the target. To facilitate this procedure, we have implemented an automated routine that, starting from the lowest gain setting for all detector channels, acquires a measurement, and determines whether the signal level is above a preselected threshold. Typically, we choose a value of 0.3 V to ensure good noise performance. In cases where the signal levels fall below this threshold, the gain setting is automatically increased to the next level and the threshold criteria is again tested. This is repeated until all measuring channels for all source locations meet the indicated threshold or until they reach the maximum gain setting. We have tested the fidelity of this scheme and found that it can correctly and reproducibly identify the appropriate gain settings, even on relatively dense media such as living tissue, and bring the signal levels for each detector to within a desirable measurement range (typically 0.3–5.0 V). The interface also allows the choosing of gain settings manually. This functionality can be used to achieve specific gain settings or to check and overwrite the results from the automated setup. Gain settings can be stored to a file and reloaded as desired.

The LABVIEW™ interface furthermore allows the real-time display of the detector data in the form of a color-encoded two-dimensional (2D) map that evolves in time as the measurement proceeds. The screen allows interactive adjustment of the chart axes and data scrolling. This feature has proven extremely useful in the development and evaluation of investigation protocols.

A variety of versions of the instrument control interface and the motor program (see Sec. II D 2) are available depending on the number of sources and detectors used in a particular application. One special operation mode of the instrument allows one to keep the source at a predetermined fixed position while performing the parallel readout of all of the detector channels at a very high rate. This allows studying fast phenomena near one source position. Currently, a 75 Hz acquisition rate is achieved in this mode. The theoretical speed limit of about 150 Hz is determined by the settling time of the detector channels.

F. Calibration

In a recent report,[18] we have described a calibration protocol that provides estimates of the relative efficiency of optical coupling between a target medium and each of the sources and detectors. These estimates are obtained from an analysis of the discrepancy between measured and anticipated responses of a homogeneous medium having regular geometry. The procedure described determines the manner in which failure to observe the expected symmetries in the detector readings can be attributed to differences in efficiency among the various measuring channels. The accounting of these differences allows for the comparison of signal intensities among the various measuring channels. Whereas this information is useful for certain computations, we wish to emphasize that such calibration is not always necessary to reconstruct dynamic behavior in the optical coefficients. In fact, the results shown here, and elsewhere, were achieved without performing any calibration. This is possible because

TABLE I. Performance characteristics of the instrument.

Parameter	Value
Detector sensitivity	10 pW (NEP)
Dynamic range	$1:10^9$ (180 dB)
Precision	CV $<1\%$, all channels
Long-term stability	$<1\%$ over 30 min
Cross talk (D-MUX)	$<1:10^{-4}$
Cross talk (detector channels)	$<1:10^{-6}$
DAQ rate	2.7 Hz at 25 sources

the data vectors used for image recovery consider only the change in response relative to a defined state (usually the temporal mean value). Thus, each detector is compared to itself, thereby avoiding the need to consider interdetector comparisons.

III. INSTRUMENT PERFORMANCE

A. System specification

Table I summarizes the most important performance characteristics of the instrument. The detector sensitivity is defined by the noise equivalent power (NEP) as determined from dark noise measurements. The dynamic range of the instrument is defined by the ratio between the NEP and the signal saturation limit. Precision and long-term stability studies have been conducted and are discussed in detail next.

Because of the large dynamic range of measurement, optical cross talk between detector channels can be important. This can occur because of light leakage within the D-MUX assembly, at the measuring head, and/or within the detection unit itself. To test for leakage within the D-MUX, we compared the measured intensities of light exiting a target vessel when light from the source fiber is and is not directed to the vessel all the while the D-MUX is illuminated by the laser source. Leakage within the D-MUX can result in light reaching the target through other fiber bundles housed in the unit. Should the degree of leakage be significant, then corresponding appreciable intensities will be recorded even when the source fiber is not directed to the target. We have observed that the cross talk value is <1 part in 10^4 for any source-detector configuration.

Cross talk within the detection unit can occur from light leakages occurring at the fiber–photodetector interfaces. This was quantified by comparing signal intensities when light from the target is directed to a detector channel and when it is not, all the while light received from the co-located source fiber (the largest signal) is directed to its detector channel. Comparison of the measured values showed that detector channel cross talk was <1 part in 10^6 for all source-detector pairs.

Figure 8 shows the result of a linearity measurement. System linearity was determined by adjusting the source light intensity using calibrated neutral density filters and recording the detector readings over a wide dynamic range. Plotted are the averaged values for the readings from the source-co-located detectors, versus the nominal optical density (OD) value.
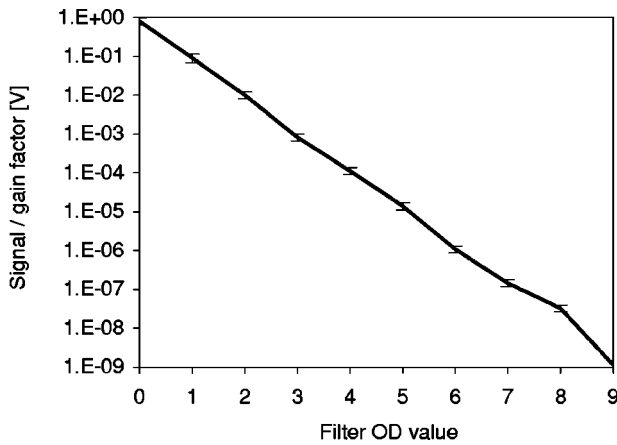
FIG. 8. Evaluation of linearity performance and dynamic range of the instrument.

Figure 9 shows the results of system precision measurements, as a function of the detector gain. The columns indicate the mean value of the coefficient of variation (CV) of the signals acquired on a homogeneous, static phantom for data collected over a 2.6 min period (500 continuous measurement points) for different gain settings (1=lowest gain and 9=highest gain); the error bars indicate the standard deviation of the CVs. For gain settings 1–6, the fluctuation in detector readings are remarkably low, with CVs well below 1.0%. In this region, the detector noise is very low and source noise contributions (laser noise, in-coupling deficiencies) dominate. At gain 7, the CV value increases to 2.5% (corresponding to a SNR of 40). At still higher gain values, the measurement precision degrades, revealing increasing signal variability. This is due to increased detector noise at higher gain settings, which limits overall measurement precision.

Figure 10 shows the result of a long-term stability study that we conducted over a period of nearly 30 min (5000 continuous measurement points). The measurements were taken on a homogeneous, static phantom having optical properties that required use of only the lowest six gain settings. Therefore, fluctuations in the signal can be attributed mainly to changes in in-coupling efficiency, laser power, and drifts in the detection electronics, rather than to detector noise. Results are presented in a bar graph format with the
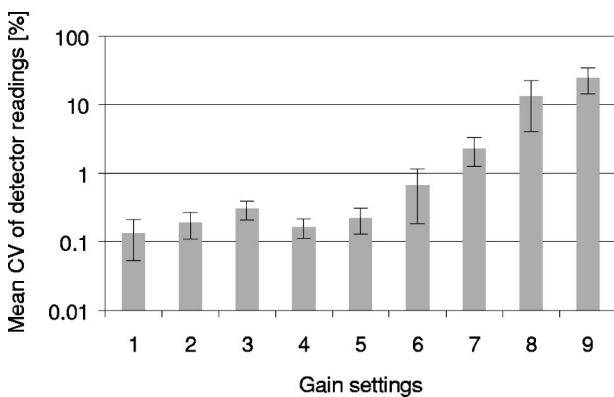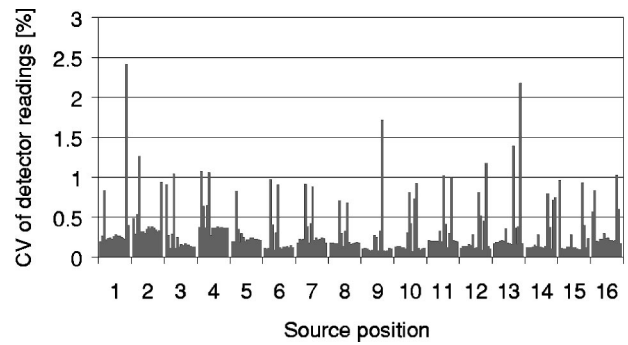

FIG. 10. Long-term stability study (5000 time points). Each group of bars represents a source position. Individual bars indicate the stability of a particular detector at that source position.

bars organized into groups according to the different source positions, with each bar representing the CV of one detector channel. This representation allows for easy identification of detector channels or source positions having notably good or bad performance. For example, the CVs of measured signals associated with source No. 4 are larger than are those for most other sources. In addition, we find that detector channels 11 and 15 tend to have slightly worse noise performance than all other detector channels. This variability reflects subtle differences in the coupling efficiencies among the various optical interfaces throughout the system. The majority of source-detector combinations show a long-term stability of better than a 1.0% CV, with most having values <0.5%.

The short-term precision of the instrument is revealed in Fig. 11, where the results of a 360-data-point phantom measurement are plotted in a bar graph similar to that in Fig. 10. Using the same gain settings as in the long-term study, most CVs are now below 0.5%.

B. Laboratory phantom studies

The purpose of these studies is to experimentally test the overall system performance and sensitivity under controlled conditions. These depend on both the quality of data collection and the stability and other characteristics of the reconstruction method. One feature of the latter that is relevant to our experimental design is the analysis of differential measurements. In practice, the differential measure of most interest to us is an instantaneous intensity relative to its temporal mean value. Thus, we have sought to collect data that

FIG. 9. Precision study: Signal variability over 500 time points as a function of detector gain.
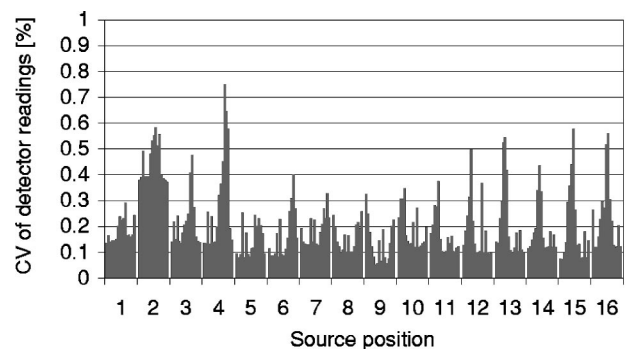

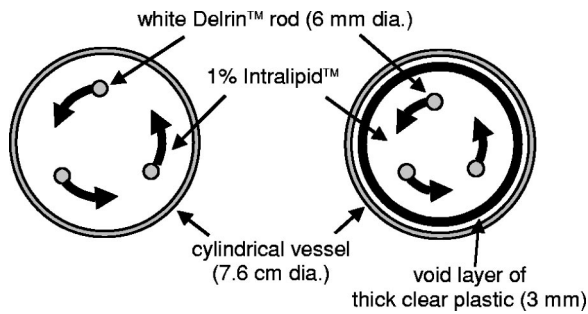FIG. 11. Short-term stability study (360 time points).

FIG. 12. Schematic of dynamic phantom used for demonstrating separation (left: case 1 w/o void, right: case 2 w/ void).

provide such information and at the same time allow for the examination of important system properties. Whereas a comprehensive examination of these is beyond the scope of this article, measures of interest we have examined include the dependence of reconstructed image quality on object location within the target vessel, the influence of more complex backgrounds, and the limits on inclusion detectability. Our approach has been to perform imaging studies on a laboratory vessel that contains various inclusions that are moved about inside the vessel while the time series image data are being collected. This simple measurement serves to document the fidelity with which inclusions contrast (i.e., $\delta\mu_a$=deviation from background absorption coefficient and δD=deviation from background diffusion coefficient) can be localized and characterized as a function of object position in the target medium relative to a fixed source-detector geometry. As a further test, we have repeated these measurements in the presence of a more complex background medium that contains a 3-mm-thick circular optical void. Our interest in this measure stems from a reported finding by Dehghani *et al.*[23] that diffusion-based imaging solvers, such as the type we employ, perform poorly under these conditions.

In an effort to a test the limits of image sensitivity, we have performed time-series tomographic measurements while stirring a 0.08-mm-diam titanium wire within the test vessel. The latter inclusion produced a maximum relative change in detector reading on the order of $\pm0.5\%$.

1. Experimental setup

A schematic of the test vessel with the added inclusions in the cross section is shown in Fig. 12. The vessel used was composed of white Delrin and measures 7.6 cm in diameter, has a height of 15 cm and a wall thickness of 2 mm. The background medium consisted of 1% (v/v) Intralipid and the
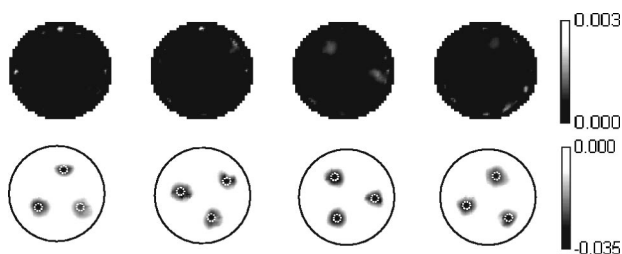

FIG. 13. The top and bottom rows are the reconstructed profiles of absorption and diffusion coefficients, respectively, from representative image frames for case 1 (w/o void).
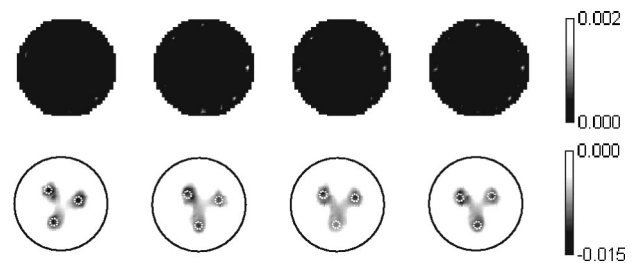

FIG. 14. The top and bottom rows are the reconstructed profiles of absorption and diffusion coefficients, respectively, from representative image frames for case 2 (w/ void).

inclusions (three rods) used were 6 mm in diameter and also composed of white Delrin. While we did not independently measure the optical properties of the inclusions, Fantini *et al.*[24] have reported values of a reduced scattering coefficient of $\mu'_s\approx12$ cm^{-1} and an absorption coefficient of $\mu_a=0.02$ cm^{-1}. These values compare to the reported[25,26] optical properties of 1% Intralipid of $\mu'_s\approx10$ cm^{-1} and $\mu_a=0.02$ cm^{-1}. This indicates that the inclusions are $\sim20\%$ more scattering than the surrounding medium. This is consistent with our detector data showing that, relative to the homogeneous background, introduction of the rods increases the intensity of light received by detectors on the same side of the vessel as the source (i.e., backreflection) and decreases the light intensity for detectors positioned on the opposite side of the vessel. Data were collected at a rate of ~3 Hz, using a 16 source$\times$16 detector arrangement positioned in a uniform circular array about the vessel, over a period of ~25 s (75 image frames).

Image recovery was achieved using the normalized constraint method recently described by Pei *et al.*[27] This algorithm is an extension of a differential analysis scheme which we refer to as the normalized difference method.[28] As we have shown, the new scheme is effective in minimizing interparameter crosstalk.[27]

We wish to emphasize that our image reconstruction efforts do not focus on the recovery of the absolute optical properties. Rather we have strived to define methods that optimize image contrast and resolution in recovering dynamic features of a target while reducing interparameter cross talk and minimizing computing time.

For all reconstruction results shown, solutions were limited to first-order computations terminated after 1000 iterations. The finite element grid used comprised 1296 elements.

2. Results

An example of the image quality recovered from phantom studies is shown in Figs. 13–15. The top row of Fig. 13
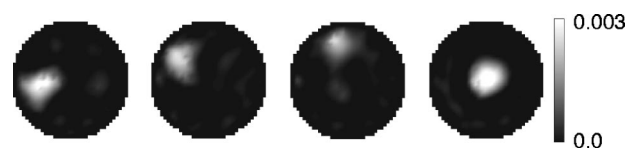

FIG. 15. Spatial maps revealing localized changes in μ_a as a function of object location. Shown are representative image frames of the reconstructed image time series of an 80-μm-diameter wire moving about in a 1%—Intralipid background.

shows the map of reconstructed changes in absorption $\delta\mu_a$ and the bottom row shows the map of recovered changes in the diffusion coefficient δD obtained at various times during the image time series. Inspection reveals that it is only in the δD map that we find evidence of the inclusions. The $\delta\mu_a$ map is essentially featureless, which is in agreement with the actual target properties. For comparison purposes, we have overlaid (dotted circles) the actual boundaries and locations of the inclusions on their recovered positions. Here again we see that these features are accurately recovered, as is the algebraic sign of the inclusions. The quantitative value of the δD contrast however is overestimated ($\sim$a factor of 7) and reflects the sensitivity of our current reconstruction scheme to errors of this type. Nevertheless, it is evident that majority of the relevant contrast features associated with the time series (object position, separation of μ_a and D, sharpness of inclusion boundaries, and algebraic sign of perturbation) are correctly recovered.

Comparison of these results to those in Fig. 14 (measurement with optical void) shows that our ability to discriminate these characteristics is not severely impaired by the presence of an intervening nonscattering layer. The location of the inclusions, separation of μ_a and D, and algebraic sign of the perturbation are all accurately recovered. Some degradation in the sharpness of the inclusion boundary is seen which may reflect either the influence of the nonscattering layer, the added difficulty of resolving more centrally positioned inclusions or both. As before, we find the quantitative value of the δD contrast is overestimated, in this case by a factor of $\sim$3. We also find, in agreement with the phantom properties, no notable contrast features in the $\delta\mu_a$ map. Note that the intervening layer itself is not seen because it does not contribute to the differential measure. This is not a fundamental limitation, but simply a function of how the particular data were acquired. Further, results in Fig. 15 reveal that even when approaching the limit of detectability, object location can still be accomplished, regardless of its position in the vessel. The object moved around in the vessel was a 0.08-mm-diam titanium wire, which produced a maximum variation in signal levels on the order of $\pm$0.5%. Here we find, however, that the inclusion size revealed in the $\delta\mu_a$ map is significantly overestimated. The latter likely reflects both the spatial resolution limits of the method and resolution limits imposed by the finite grid size used.

IV. DISCUSSION

A. Comparison of other reported measuring systems

As evidenced by the increasing number of reports in the literature, an interest in developing practical measuring systems for optical tomography remains high. It is instructive to make a specific comparison of this literature. The performance characteristics of systems recently reported are listed in Table II. Proceeding from the left- to right-hand side, the systems are organized according to different data collection modes; cw, frequency domain, and time resolved. Also listed are significant performance characteristics such as photosensitivity, number of source-detector sites, dynamic range, acquisition speed, and tomographic measurement strategies.

The system featuring the highest sensitivity and most informative measurement data is that described by Schmidt et al.[10] These authors developed a single photon counting, time-resolved measuring system incorporating 32 by 32 source-detector sites. Tomographic measurements are achieved by time multiplexing a single illuminating source together with parallel multichannel detection. The dynamic measuring range can be extended by three decades using a variable optical attenuator. While fast data collection was not a specific design objective for this system, the selected detection scheme nevertheless limits data collection rates to approximately 1 Hz. In addition, the need to avoid nonlinear detector responses effectively imposes an upper limit on source intensity while also reducing the view angle of measurement. A system employing a similar measurement strategy (eight source, two detectors, and two wavelengths) being used for simultaneous magnetic resonance imaging (MRI) studies has been described by Ntziachristos et al.[9,29]

Systems based on frequency-domain measurements are described by Franceschini et al.[4] and Pogue et al.[2,30] Both collect tomographic data by time multiplexing the source and use of a photomultiplier tube (PMT) as a detector. The system by Pogue et al.[2,30] is applied to collect full view measurements and, hence, has the need to extend the dynamic measurement range. This is achieved using a variable filter wheel. A more recent version of their basic system employs multiple PMT's to allow for parallel data collection.[31] Image-frame acquisition rates are notably faster with the system used in Ref. 4 (model 96208 Oximeter, available from ISS, Inc., Champaign, IL). This is achieved using electronic time-multiplexing schemes of the sources and operating two PMT's parallel at a smaller, fixed dynamic range.

Several reports, including the current one, have adopted CW measurement schemes. Typically, these systems are more economical as they require less sophisticated electronics to achieve signal detection. Another feature that several groups, including ours, have adopted is the use of frequency encoding methods to allow for simultaneous multiwavelength detection. This option is not available in the case of single photon counting. As we have recently discussed,[18] the use of this strategy to provide parallel multisite source illumination—as used in Ref. 14—can significantly limit the achievable dynamic range. We have avoided this by limiting the use of this technique to provide source discrimination for only one measuring site at a time. As noted in the text, we achieve a large dynamic range by introducing gain switching. The approach we have adopted is similar to the technique used by Colak et al.[1] Where we differ in functionality with the latter system is in the use of a fast optomechanical source switch combined with the already noted use of frequency encoding techniques. Colak et al.[1] achieve wavelength discrimination by time-multiplexing different lasers. Thus, whereas both systems employ parallel detection, we can achieve much faster framing rates and even faster data acquisition rates (540 vs 2100–8600 Hz) even though the system by Colak et al.[1] employs a much higher source-detector density.

TABLE II. Comparison of optical tomography instruments recently developed for human studies. The acronyms used herein are defined as follows: CW: continuous wave, TR: time resolved, FD: frequency domain, APD: avalanche photodiode, SiPD: silicon photodiode, pin PD: p-i-n photodiode, PMT: photomultiplier tube, MCP-PMT: multichannel plate-photomultiplier tube, NEP: noise equivalent power, VOA: variable optical attenuator, FE: frequency encoded, TM: time multiplexed, PA: parallel.

Instrument described by	Yamashita et al.	Siegel et al.	Colak et al.	Schmitz et al.	Franceschini et al.	Pogue et al.	Schmidt et al.
Method	CW	CW	CW	CW	FD	FD	TR
Reference No.	16	14	1		4	2	10
No. source pos. (S)/ No. detector pos. (D)	8 S/8 D	9 S/8 D	225 S/225 D	25 S/32 D	16 S/2 D	16 S/16 D	32 S/32 D
No. of wavelengths	2	2	3	1–4	2	1	1
Photodetector	APD	SiPD	pin PD	SiPD	PMT	PMT	MCP-PMT single photon
Sensitivity (NEP)	60 fW	40 pW	25 fW	10 pW	~fW	<fW	60 dB VOA
Dynamic range detection	120 dB	92 dB	192 dB	180 dB	96 dB	160 dB	1024
Data points[a]	128	144	~195 000	800–3200	64	256	~1
Data rate[b] (Hz)	256	72	~540	2160–8640	400	~0.6[d]	
Acquisition time[c]	0.5 s	2 s	~6 min	0.37 s	0.16 s	7 min[d]	10–20 min
Operation	FE source position FE wavelengths PA detection	FE source position FE wavelengths PA detection	TM source position TM wavelengths PA detection	TM source position FE wavelengths PA detection	TM source position TM wavelengths PA detection	TM source position TM detection[d]	TM source position PA detection
Measuring geometry, applications	Planar, transcranial topography	Planar, cerebral hemodynamics	Fixed cup, mammography	Multipurpose	Planar, cerebral hemodynamics	Circular, mammography	Circular, cerebral hemorrhage

[a]Denotes independent measurements (S×D× No. of wavelengths).
[b]Denotes data points per second.
[c]As per complete set of data points.
[d]Recently introduced PA detection accelerates DAQ by a factor of ~16.

B. Applications for dynamic imaging

Here, we described our efforts to implement a practical measuring system well suited to characterize the time dependence of optical contrast features in highly scattering media. Motivating this work is the hypothesis that optical tomography, adapted to provide a time series of image data, can allow for the examination of a large untapped reservoir of knowledge regarding tissue function—the spatiotemporal dynamics of the vascular response and hemoglobin states.[6,7,18,20] The details of this control—how it is influenced by disease, trauma or pharmacoactive agents—is currently known by only the grossest of ways. Significantly, whereas the techniques available to characterize these details have been lacking, at least as applied to large tissue structures, it is nevertheless well appreciated that important functionalities of the vasculature are easily discerned in accordance to their temporal response. Thus, it is the case that the detection of a time varying signal equal to the rate of ventricular concentration in the periphery can be reliably taken as originating from arterial structures. A similar assignment can be made principally between the respiratory frequency and the veins, and the vasomotor frequency and the microvessels. As we have recently emphasized,[6] such well-defined structure-response features allow for the generation of spatial maps that assign distinct functional responses to anatomical structures. Supporting this assignment is the simple observation that, in the near infrared region, it is essentially only the hemoglobin signal that exhibits natural time variability. Also aiding the practical utility of these measures is the finding that the temporal variations in optical properties can be characterized with much greater fidelity than can corresponding efforts to recover the optical coefficients themselves.[20]

C. Future developments

One issue emphasized in the literature having particular significance for practical studies is the need for a robust calibration scheme.[32] As we have indicated, depending on the type of information sought, it is not always necessary to perform a calibration. In instances where it is important, the scheme we have implemented makes use of expected symmetries from a homogeneous target. The strategy used is applicable to problems having, for example, approximately cylindrical (e.g., limbs), hemispherical (e.g., breast), or spherical geometries (head model). While the details of this are beyond the scope of this discussion, and will be reported elsewhere, we simply point out that the essence of the technique divides the system of equations corresponding to the 3D calibration problem into a set of smaller 2D problems each of which is individually solved in the same manner as described previously.[18] The final determination of coefficients, however, requires additional operations that link the results from the individual subproblems.

Another feature of system functionality, where room for additional development remains, concerns its real-time capability. As noted in the text, the instrument described can display the measured time varying source-detector responses as they are collected. We have found this capability especially useful in our efforts to develop provocation protocols. An

even more useful feature would be to reconstruct and display 3D image results in real time. Recently, we have achieved the latter capability using a diffusion-based algebraic reconstruction solver[28] and are currently developing software to allow for interactive volume rendering as the image data is computed on the fly. We note that in optical studies the size of the image data sets is much smaller (typically <10 000 unknowns/frame) than in MRI studies, which significantly limits the computational needs for image display.

Finally, it is worth emphasizing that the ability to study and characterize dynamic processes in highly scattering media is not a capability easily accomplished using other measuring technologies. As noted in the Introduction, our principal aim has been to apply the described system for the study of vascular states in living tissue. We recognize, however, that other application areas may also find the described capability useful. One such area involves the mixing of powders, which is a process important in the chemical and pharmaceutical industries. For instance, it is known that mixing for longer times does not necessarily produce better results, and can in fact lead to the resegregation of components. Information obtained by monitoring the dynamics of the moving solids and voids in a cross sectional view might lead to the devising of protocols that lead to more reproducible pharmaceutical formulations.

ACKNOWLEDGMENTS

[1] S. B. Colak, M. B. van der Mark, G. W. 't Hooft, J. H. Hoogenraad, E. S. van der Linden, and F. A. Kuijpers, IEEE J. Sel. Top. Quantum Electron. **5**, 1143 (1999).

[2] B. W. Pogue, M. Testorf, T. Mcbride, U. Österberg, and K. Paulsen, Opt. Express **1**, 391 (1997).

[3] A. Villringer and B. Chance, Trends Neurosci. **20**, 435 (1997).

[4] M. A. Franceschini, E. Gratton, S. Fantini, V. Toronov, and M. Filiaci, Opt. Express **6**, 49 (2000).

[5] D. A. Benaron, S. R. Hintz, A. Villringer, D. Boas, A. Kleinschmidt, J. Frahm, C. Hirth, H. Obrig, J. C. Van Houten, E. L. Kermit, W. Cheong, and D. K. Stevenson, J. Cereb. Blood Flow Metab. **20**, 469 (2000).

[6] G. S. Landis, T. F. Panetta, S. B. Blattman, H. L. Graber, Y. Pei, C. H. Schmitz, and R. L. Barbour, Proc. SPIE **4250**, 130 (2001).

[7] R. L. Barbour, H. L. Graber, Y. Pei, and C. H. Schmitz, Proc. SPIE **4250**, 577 (2001).

[8] A. Klose, A. H. Hielscher, K. M. Hanson, and J. Beuthan, Proc. SPIE **3566**, 151 (1998).

[9] V. Ntziachristos, X. Ma, M. Schnall, A. G. Yodh, and B. Chance, OSA Trends Opt. Photonics Ser. **21**, 284 (1998).

[10] F. E. W. Schmidt, M. E. Fry, E. M. C. Hillman, J. C. Hebden, and D. T. Delpy, Rev. Sci. Instrum. **71**, 256 (2000).

[11] H. Jiang, K. D. Paulsen, U. L. Osterberg, B. W. Pogue, and M. S. Patterson, J. Opt. Soc. Am. A **13**, 253 (1996).

[12] J. S. Reynolds, T. L. Troy, and E. M. Sevick-Muraca, Biotechnol. Prog. **13**, 669 (1997).

[13] M. A. Franceschini, K. T. Moesta, S. Fantini, G. Gaida, E. Gratton, H. Jess, W. Mantulin, M. Seeber, P. M. Schlag, and M. Kaschke, Proc. Natl. Acad. Sci. U.S.A. **94**, 6468 (1997).

[14] A. M. Siegel, J. J. A. Marota, and D. A. Boas, Opt. Express **4**, 287 (1999).

[15] S. Zhao, M. A. O'Leary, S. Nioka, and B. Chance, Proc. SPIE **2389**, 809 (1995).

[16] Y. Yamashita, A. Maki, and H. Koizumi, J. Biomed. Opt. **4**, 414 (1999).

[17] R. L. Barbour, R. Andronica, Q. Sha, H. L. Graber, and I. Soller, OSA Trends Opt. Photonics Ser. **21**, 251 (1998).

[18] C. H. Schmitz, H. L. Graber, H. Luo, I. Arif, J. Hira, Y. Pei, A. Bluestone, S. Zhong, R. Andronica, I. Soller, N. Ramirez, S.-L. S. Barbour, and R. L. Barbour, Appl. Opt. **39**, 6466 (2000).

[19] J. C. Hebden, S. R. Arridge, and D. T. Delpy, Phys. Med. Biol. **42**, 825 (1997).

[20] R. L. Barbour, H. L. Graber, Y. Pei, S. Zhong, and C. H. Schmitz, J. Opt. Soc. Am. A **18**, 3018 (2001).

[21] C. H. Schmitz, M. Löcker, J. Lasker, A. H. Hielscher, and R. L. Barbour, Proc. SPIE **4250**, 171 (2001).

[22] C. H. Schmitz, Y. Pei, H. L. Graber, J. M. Lasker, A. H. Hielscher, and R. L. Barbour, Proc. SPIE **4431**, 282 (2001).

[23] H. Dehghani, S. R. Arridge, M. Schweiger, and D. T. Delpy, J. Opt. Soc. Am. A **17**, 1659 (2000).

[24] S. Fantini, M. A. Franceschini, G. Gaida, H. Jess, H. Erdl, W. W. Mantulin, E. Gratton, K. T. Moesta, P. M. Schlag, and M. Kaschke, OSA Trends Opt. Photonics Ser. **2**, 160 (1996).

[25] H. J. van Staveren, C. J. M. Moes, J. van Marle, S. A. Prahl, and M. J. C. van Gemert, Appl. Opt. **30**, 4507 (1991).

[26] G. M. Hale and M. R. Querry, Appl. Opt. **12**, 555 (1973).

[27] Y. Pei, H. L. Graber, and R. L. Barbour, Opt. Express **9**, 97 (2001).

[28] Y. Pei, H. L. Graber, and R. L. Barbour, Appl. Opt. **40**, 5755 (2001).

[29] V. Ntziachristos, X. Ma, and Britton Chance, Rev. Sci. Instrum. **69**, 4221 (1998).

[30] B. W. Pogue, S. P. Poplack, T. O. McBride, W. A. Wells, K. S. Osterman, U. L. Österberg, and K. D. Paulsen, Radiology **218**, 261 (2001).

[31] T. O. McBride, B. W. Pogue, S. Jiang, U. L. Österberg, and K. D. Paulsen, Rev. Sci. Instrum. **72**, 1817 (2001).

[32] D. A. Boas, T. Gaudette, and S. R. Arridge, Opt. Express **8**, 263 (2001).